Computational and Experimental Determination of the Properties, Structure, and Stability of Peptoid Nanosheets and Nanotubes

Mingfei Zhao,[†,‖] Shuai Zhang,[‡,¶] Renyu Zheng,[§,¶] Sarah Alamdari,[§] Christopher J. Mundy,[¶,§] Jim Pfaendtner,[§,¶] Lilo D. Pozzo,[§] Chun-Long Chen,[¶,§] James J. De Yoreo,[¶,‡] and Andrew L. Ferguson[∗,†]

†*Pritzker School of Molecular Engineering, University of Chicago, Chicago, Illinois 60637, USA*

‡*Materials Science and Engineering, University of Washington, Seattle, Washington 98195, USA*

¶*Physical Sciences Division, Pacific Northwest National Laboratory, Richmond, Washington 99354, USA*

§*Department of Chemical Engineering, University of Washington, Seattle, Washington 98195, USA*

‖*Present Address: Theoretical Biology and Biophysics Group, Los Alamos National Laboratory, Los Alamos, New Mexico 87545, USA*

E-mail: andrewferguson@uchicago.edu

Abstract

Peptoids (N-substituted glycines) are a group of highly controllable peptidomimetic polymers. Amphiphilic diblock peptoids have been engineered to assemble crystalline nanospheres, nanofibrils, nanosheets, and nanotubes with biochemical, biomedical, and bioengineering applications. The mechanical properties of peptoid nanoaggregates and their relationship to the emergent self-assembled morphologies have been relatively unexplored and are critical for the rational design of peptoid nanomaterials. In this work, we consider a family of amphiphilic diblock peptoids consisting of a prototypical tube-former – Nbrpm6Nc6, a NH_2 capped hydrophobic block of six N-((4-bromophenyl)methyl)glycine residues conjugated to a polar $NH_3(CH_2)_5CO$ tail – a prototypical sheet-former – Nbrpe6Nc6, where the hydrophobic block comprises six N-((4-bromophenyl)ethyl)glycine residues – and an intermediate sequence that forms mixed structures – (NbrpeNbrpm)3Nc6. We combine all-atom molecular dynamics simulations and atomic force microscopy to determine the mechanical properties of the self-assembled 2D crystalline nanosheets and relate these properties to the observed self-assembled morphologies. We find good agreement between our computational predictions and experimental measurements of Young's modulus of crystalline nanosheets. A computational analysis of the bending modulus along the two axes of the planar crystalline nanosheets reveals bending to be more favorable along the axis in which the peptoids stack by interdigitation of the side chains compared to that in which they form columnar crystals with pi-stacked side chains. We construct molecular models of nanotubes of the Nbrpm6Nc6 tube-forming peptoid and predict a stability optimum in good agreement with experimental measurements. A theoretical model of nanotube stability suggests that this optimum is a free energy minimum corresponding to a "Goldilocks" tube radius at which capillary wave fluctuations in the tube wall are minimized.

1 Introduction

Peptoids (N-substituted glycines) are a group of promising peptidomimetic polymers that are regioisomers of natural peptides. Peptoids have been proposed as promising biomimetic and biocompatible molecular materials that have recently found applications in numerous biochemical, biomedical, and bioengineering applications.[1–5,5–18] Peptoids possess a similar chemical structure to natural peptides, but are differentiated by the attachment of the peptoid side chain to the amide nitrogen rather than the α-carbon, as is the case in natural peptides.[7] This structural modification leads to large changes in the molecular properties of peptoids relative to peptides due to elimination of the α-carbon chiral center, loss of $-$NH hydrogen bond donors, accessibility of backbone ω dihedral *cis*/*trans* isomerizations, and resistance to recognition and degradation by proteolytic enzymes.[3,7,11,19,20] Peptoid synthesis is cheap, easy, and precisely controllable[3,21,22] and has been used to fabricate peptoids capable of self-assembling into diverse supramolecular morphologies such as spheres, helices, tubes, cylinders, ribbons, bilayers, and sheets.[7,17,19,23–33]

Self-assembled crystalline peptoid nanotubes were first reported by Vollrath et al. in 2013.[34] Since then, they have drawn substantial research interest into their molecular structure, materials properties, and potential technological applications.[15,35–38] The first peptoid nanotubes were composed from columnar stacks of cyclic peptoids,[34] but more recently peptoid nanotubes and nanosheets have been produced from amphiphilic peptoid chains containing alternating[14,28] or diblock[15,19,35–40] arrangements of hydrophilic and hydrophobic components. Self-assembly of peptoid nanotubes assembled from short amphiphilic sequences has been observed in experiments through a putative sheet-to-tube transition.[38] Models for the structure of the peptoid nanotubes have been proposed,[38] but their atomic-level structures have never been fully resolved and significant questions remain unanswered. Do the elastic properties of planar nanosheets dictate the propensity for particular peptoid sequences to form nanotubes rather than nanosheets? What is the molecular structure of a nanotube, is it simply a rolled up nanosheet? What controls the preferred axial direction for rolling of the nanosheet into a nanotube? What is the origin of the observed tight distribution in nanotube radii?

In this work, we conduct all-atom molecular dynamics (MD) simulations and atomic force microscopy (AFM) measurements to determine the mechanical properties of peptoid tubes and sheets and relate these to the supramolecular structure of the self-assembled morphologies. We consider a family of three amphiphilic diblock peptoids: Nbrpe6Nc6, (NbrpeNbrpm)3Nc6, and Nbrpm6Nc6. Nbrpe and Nbrpm represent, respectively, NH_2 capped hydrophobic blocks of six N-((4-bromophenyl)methyl)glycine and N-((4-bromophenyl)ethyl)glycine residues, while Nc6 is a polar 6-aminohexanoic acid ($NH_3(CH_2)_5CO$) tail (Fig. 1). Nbrpe6Nc6 is a prototypical sheet-forming sequence[19,39,41–43] that we observe to form molecularly-thin extended nanosheets with linear extents of approximately 1-3 μm (Fig. 1a). Nbrpm6Nc6 is a prototypical tube-forming sequence[37,38,44] that we observe to assemble nanotubes with an approximate radius of ~20 nm (Fig. 1b). Jin et al. previously studied the closely related Nbrpm6Nce6 sequence – where the polar Nce6 tail comprises six N-(2-carboxyethyl) glycine repeats – and reported a diameter distribution of (37.2 ± 2.7) nm over 50 nanotubes imaged by transmission electron microscopy (TEM), corresponding to a similar characteristic radius of ~19 nm.[38] (NbrpeNbrpm)3Nc6 is a mixed sequence that forms mixed structures of planar nanosheets, sheets with curved edges, and twisted fibrils (Fig. 1c).

Our primary findings for these three systems are as follows. Our computational predictions and experimental measurements of the Young's moduli of Nbrpe6Nc6 and (NbrpeNbrpm)3Nc6 planar peptoid sheets are in good agreement, lending confidence to our computational predictions of the directionally-resolved bending moduli and Young's modulus measurement of Nbrpm6Nc6 sheets that, as a tube forming sequence, are not readily accessible to experiment. We predict a substantially lower bending modulus along one axis of the nanosheet that suggesting an axial preference for the formation of nanotubes along that axis in which the peptoids stack by interdigitation of the side chains compared to that in which they form columnar crystals with pi-stacked side chains. Molecular simulations of a nanotube

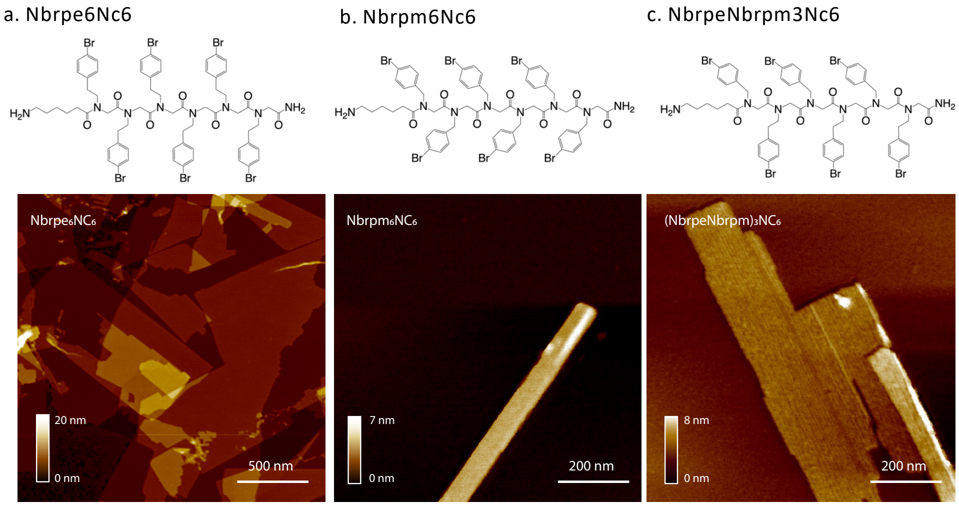

a. Nbrpe6Nc6

b. Nbrpm6Nc6

c. NbrpeNbrpm3Nc6

d. Nbrpe6Nc6 nanosheets

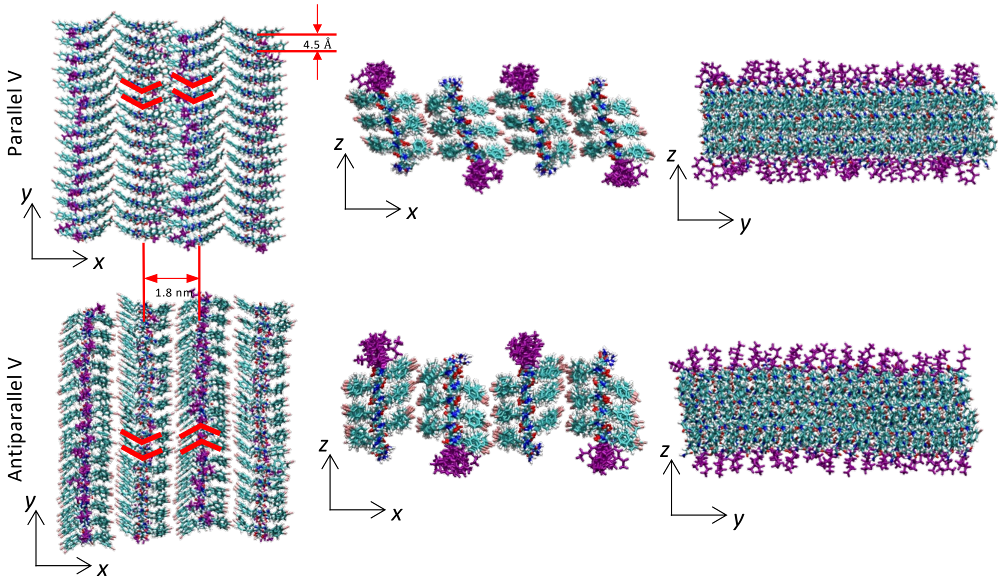

Figure 1: AFM images of self-assembled peptoid nanostructures formed by slow solvent evaporation. (a) Nbrpe6Nc6 – a NH_2 capped hydrophobic block of six N-((4-bromophenyl)ethyl)glycine residues conjugated to a polar $NH_3(CH_2)_5CO$ tail – spontaneously assembles into molecularly-thin planar crystalline nanosheets. (b) Nbrpm6Nc6 – a NH_2 capped hydrophobic block of six N-((4-bromophenyl)methyl)glycine residues conjugated to a polar $NH_3(CH_2)_5CO$ tail – assembles into nanotubes with an approxiamte radius of ∼20 nm. (c) (NbrpeNbrpm)3Nc6 – a mixed sequence – forms mixed structures including planar nanosheets, sheets with curved edges, and twisted fibrils. Here we show an example of striped nanosheets with curved edges. (d) Molecular structure of crystalline planar nanosheets in parallel V and anti-parallel V configurations.[19] Schematic Vs are superposed on the molecular models to highlight the packing differences. To help distinguish the component parts of the peptoid molecules, the Nbrpe6 blocks are colored based on their atom types while the Nc6 tails are colored in purple. Peptoid nanotubes have been proposed to form by a putative sheet-to-tube transition in which nanosheets roll up along their x-axis.[38]

produce a structure in good agreement with prior models,[38] but suggest that the structure is not simply a rolled-up nanosheet and possesses subtle differences in the molecular details of the side chain packing in the tube wall. A theoretical model of nanotube stability provides a molecular-level rationalization for the peaked distribution of Nbrpm6Nc6 nanotubes observed in experiment as the result of a free energy minimum resulting from minimization of capillary wave fluctuations in the tube wall. Our results bridge understanding of the materials properties of peptoid nanoaggregates and new precepts for the design and control of peptoid nanomaterials.

2 Materials and Methods

2.1 Solid-phase peptoid synthesis

Nbrpe6Nc6, (NbrpeNbrpm)3Nc6, and Nbrpm6Nc6 peptoids were synthesized using an Aappatec Apex 396 robotic synthesizer using a solid-phase submonomer synthesis procedure detailed in Refs.[21,38,39] Product peptoids were cleaved from the resin using 95% aqueous solution of trifluoroacetic acid (TFA). Purification was then conducted using preparative high performance liquid chromatography (prep-HPLC) and the purified product confirmed using a Waters ACQUITY reverse-phase ultra performance liquid chromatograph (UPLC) and a Waters SQD2 mass spectrometer. The terminal purified peptoid was lyophilized twice and stored as a powder at (-80)°C.

2.2 Evaporation-induced assembly of nanosheets and nanotubes

Peptoids were induced to self-assemble into nanosheets and nanotubes using an evaporative assembly procedure detailed in Refs.[38,39] The lyophilized powder of peptoids was hydrated in 50:50 v/v acetonitrile/water solution to a concentration of 5.0 mM, and the organic component evaporated at 4°C over the course of seven days.

2.3 Atomic force microscopy (AFM) nanomechanical measurement

The peptoid assembly solution was diluted 20-40 times in water. Then 20 μl diluted peptoid solution was deposited onto freshly cleaved muscovite mica (Ted Pella, CA) and incubated for 20 min. Later the mica surface was rinsed with 100 ul water (Ambion, Thermo Fisher Scientific) and characterized in water with ScayAsyst-Fluid+ AFM probes (Bruker, CA) using MultiMode VIII AFM (Bruker, CA) in PeakForce QNM mode. Before the nanomechanical measurement, the AFM cantilever and AFM hardware were calibrated with the protocol in the user manual from Bruker. The raw data were further analyzed by offline software, Nanoscope Analysis v1.5 (Bruker, CA).

2.4 All-atom molecular dynamics (MD) simulations

All-atom molecular models of peptoids. The three amphiphilic diblock peptoids considered in this work – Nbrpe6Nc6, (NbrpeNbrpm)3Nc6, and Nbrpm6Nc6 – comprise three molecular building blocks: a hydrophobic N-((4-bromophenyl)ethyl)glycine residue (Nbrpe), a hydrophobic N-((4-bromophenyl)methyl)glycine residue (Nbrpm), and a polar $NH_3(CH_2)_5CO$ (Nc6) tail. Peptoid sequences are constructed using Avogadro 1.2.0,[45] and modeled using the improved all-atom CGenFF peptoid force field developed by Weiser and Santiso as a peptoid-tuned modification of the CHARMM22 peptide force field.[46–48] We observe that alternative choices of force field exist, including the MFTOID model[49] and the DREIDING-based PEPDROID model .[50] Experimentally, peptoid assembly typically proceeds by dissolution in an organic solvent/water mixture and then slowly evaporating the organic phase to induce hydrophobic association into the terminal nanoaggregates that are the thermodynamically stable state in the final pure water solvent.[19,30,38–41] We have previously explored the mechanistic pathways for the self-assembly of crystalline peptoid sheets as a function of solvent quality,[41] but in this work we model only the terminal self-assembled nanoaggregates in a pure water environment. The amine group at the end of the Nc6 alkyl chain is assumed to be fully protonated as $-NH_3^+$ within the water solvent at pH 7. The pKa of the Nc6 terminal amine estimated from hexylamine is ∼10.8,[51] leading us to model it as protonated. While it is possible to model the dynamic equilibrium and context dependence of protonation state using reactive force fields [52] or constant pH simulations ,[53] these approaches remain too computationally expensive to permit access to the microsecond time scales required by this work and so we fix the protonation state of ionizable groups. Water was modeled using the TIP3P model.[54] Initial system configurations were generated using Packmol.[55] All-atom MD simulations were performed in Gromacs 2019.2.[56,57] Forces in excess of 1000 kJ/mol.nm in the initial state of the system were removed through steepest descent energy minimization. Initial atom velocities were assigned from a Maxwell-Boltzmann distribution at 300 K. Periodic boundary conditions were applied in all three dimensions. Unless otherwise stated, systems were first equilibrated for 200 ps in the NPT ensemble at 300 K and 1 bar employing a velocity rescaling thermostat[58] with a time constant of 0.1 ps and a Berendsen barostat[59] with a time constant of 1.0 ps and compressibility of 4.5×10^{-5} bar^{-1}, then subjected to production runs of 1 μs or more in the NPT ensemble at 300 K and 1 bar employing a Nosé-Hoover thermostat[60] with a time constant of 1.0 ps and Parrinello-Rahman barostat[61] with a time constant of 1.0 ps and compressibility of 4.5×10^{-5} bar^{-1}. The equations of motion were numerically integrated using a leap-frog algorithm[62] with 2 fs time step. The LINCS algorithm was used to fix the length of covalent bonds involving hydrogen.[63] Lennard-Jones interactions were shifted smoothly to zero at a 1.2 nm cutoff. Electrostatics were modeled using particle mesh Ewald summation[64] with a real-space cutoff of 1.0 nm and 0.16 nm Fourier grid spacing that were optimized during runtime. Simulation snapshots were saved for analysis at a 10 ps save rate. Simulation trajectories were visualized using VMD.[65]

Construction of planar crystalline nanosheets. Initial coordinates of Nbrpe6Nc6, (NbrpeNbrpm)3Nc6, and Nbrpm6Nc6 peptoid monomers within planar crystalline nanosheets were generated using an approach previously detailed in Ref.[41] Planar crystals were constructed from a single layer of peptoid monomers elongated in the z-dimension based on the “parallel V” and “anti-parallel V” structures reported by Xuan et al. (cf. Figs. 2 and 3, therein).[19] Our prior simulation studies have shown the *trans* ($\omega = 180°$) state of the ω backbone dihedrals to be the stable isomer of this torsional angle within a crystalline nanosheets.[41] Nanosheets are periodic in the x and y dimensions. We define the x-dimension as the axis along which peptoids stack by interdigitation of the side chains and the y-dimension as that in which they form columnar crystals with pi-stacking of the aromatic rings of the side chains.

For the purposes of calculating the Young's modulus Y by simulated nanoindentation (*vide infra*), we constructed approximately square nanosheets constructed from columns of 28 monomers stacked in the y-direction with a 0.45 nm spacing between peptoids, which themselves are elongated in the z-dimension. Eight such columns were then assembled in the x-dimension with a 1.8 nm spacing between each stack. The directionality of each y-stack was maintained constant between all stacks to form a nanosheet in the parallel V configuration, or alternated to assemble a sheet in the anti-parallel V configuration (cf. Fig. 1d). Nanosheets were placed in a $(14.2 \times 14.2 \times 9.5)$ nm^3 box and solvated with 50,250 water molecules at a density of $\sim$1 g/cm^3 and 224 OH$^-$ ions to maintain charge neutrality. The z dimension of the box was sufficiently large that the sheet did not directly interact with its own periodic image through the periodic boundaries in z. We verified that our calculations did not suffer from finite size effects by confirming agreement with predictions computed for sheets with 43% larger areas.

A similar construction protocol was followed to construct nanosheets used to compute directionally-resolved bending moduli in x and y by applying uniaxial deformations (*vide infra*). For calculation of the x bending modulus Y_x, we assembled columns of eight monomers in the y-dimension and packed five such columns in the x-dimension in either a parallel V or anti-parallel V configuration. Nanosheets were placed in a $(10 \times 3.6 \times 7.2)$ nm^3 box and solvated with 8,300 water molecules at a density of $\sim$1 g/cm^3 and 42 OH$^-$ ions to maintain charge neutrality. For calculation of the y bending modulus Y_y, we assembled columns of 22 monomers in the y-dimension and packed two such columns in the x-dimension in either a parallel V or anti-parallel V configuration. Nanosheets were placed in a $(10 \times 3.6 \times 7.2)$ nm^3

box and solvated with 8,300 water molecules at a density of $\sim$1 g/cm^3 and 44 OH$^-$ ions to maintain charge neutrality. We verified that our calculations did not suffer from finite size effects by confirming agreement with predictions computed in boxes 50% larger along the bending dimension.

To relax the initial configuration of the planar nanosheets, we employed a multi-stage equilibration protocol in the semi-isotropic NPT ensemble.[41] We heated the systems from 0 K to 300 K in increments of 50 K over the course of 30 ps using a velocity rescaling thermostat[58] with a time constant of 0.1 ps, and maintained the pressure at 1 bar using a Berendsen barostat[59] with a time constant of 1.0 ps and compressibility of 4.5×10^{-5} bar^{-1} for the independently coupled xy and z dimensions. We then performed relaxation runs of 1 μs in the semi-isotropic NPT ensemble at 300 K and 1 bar employing a Nosé-Hoover thermostat[60] with a time constant of 1.0 ps and Parrinello-Rahman barostat[61] with a time constant of 1.0 ps and compressibility of 4.5×10^{-5} bar^{-1} for the xy and z dimensions. Young's modulus and directional bending moduli calculations were performed on the relaxed nanosheets in the terminal frame of the relaxation run.

Construction of Nbrpm6Nc6 nanotubes. Nanotubes assembled from diblock amphiphilic peptoids have been speculated to form by a putative sheet-to-tube transition, in which a nanosheet rolls up along its x-axis.[38] The sheet-to-tube transition is known experimentally to require hours to days to complete,[38] meaning that it lies far outside the time scales of molecular dynamics simulations and that it is intractable to simulate the transition directly. Instead, we constructed initial molecular models for a cylindrical nanotube formed by the Nbrpm6Nc6 tube-forming sequence by excising from the relaxed structure of the planar crystalline nanosheets after the 1 μs relaxation run a small unit cell comprising six columnar monomers stacked in y and two such columns stacked together in x (Fig. 4). We assembled copies of this unit cell into a circular geometry with the y-stacked columns lying along the long axis of the nanotube at separations of 1.48 nm to generate cylindrical slices of the nanotube in the xz plane in either a parallel V or anti-parallel V manner and mimicking the molecular geometry proposed in Ref.[38] By varying the number of y-stacks comprising the circumference of the cylinder between 64-88, we modeled nanotubes with radii of approximately R = 15-20 nm. Nanotubes were placed in cubic simulation boxes of dimensions in the range $(39.8 \times 39.8 \times 3)$ – $(51.1 \times 51.1 \times 3)$ nm^3, depending on the radius of the nanotube. Periodic boundary conditions were applied in all three dimensions and we ensured that the x and z dimensions were sufficiently large to prevent direct interactions of the nanotube with its own periodic images through the x and z periodic walls. The system was solvated with 130,719-222,356 water molecules to a density of $\sim$1 g/cm^3 and 384-528 OH^- ions to maintain charge neutrality. It was ensured that the local water density inside and outside of the tube was equal since the topology of the simulation means that there is no possibility for water exchange over the tube wall.

We employed a multi-stage equilibration protocol in the semi-isotropic NPT ensemble to relax the nanotubes.[41] We heated the systems from 0 K to 300 K in increments of 50 K over the course of 30 ps using a velocity rescaling thermostat[58] with a time constant of 0.1 ps, and maintained the pressure at 1 bar using a Berendsen barostat[59] with a time constant of 1.0 ps and compressibility of 4.5×10^{-5} bar^{-1} for the independently coupled xz and y dimensions. Relaxation runs of 10 ns were conducted in the semi-isotropic NPT ensemble at 300 K and 1 bar employing a Nosé-Hoover thermostat[60] with a time constant of 1.0 ps and Parrinello-Rahman barostat[61] with a time constant of 1.0 ps and compressibility of 4.5×10^{-5} bar^{-1} for the xz and y dimensions.

We found that the initial nanotubes assembled by this procedure tended to exhibit structural instabilities and develop defects within the tube wall wherein neighboring columns shift out of register. Accordingly, we iteratively repeated the nanotube construction protocol multiple times by identifying the smoothest portion of the nanotube wall and extracting a new two-column unit cell from this portion of the cylindrical cross section. This unit cell was then used to build the coordinates of a new nanotube using the procedure described above. Importantly, we also re-solvated the newly constructed tube ensuring equal local water density of ~1 g/cm^3 inside and outside the tube. In general, we had to perform approximately three iterations of this process to achieve unit cells with a fixed structure that produced defect-free nanotubes. The terminal unit cell resulting from this iterative process differs between the parallel V and anti-parallel V morphologies but is well-conserved among nanotubes of all radii considered in this work (Fig. 4). The nanotube unit cells differ from those found in the planar nanosheets (Fig. 1d) in terms of the relative tilting of the columns that make an angles of approximately 5-20° with the z-axis and the offset in the interdigitated packing of side chains between adjacent columns in the nanotube wall.

Computational prediction of nanosheet Young's moduli by simulated nanoindentation. We predicted the Young's moduli Y of the planar crystalline nanosheets by computationally mimicking the experimental nanoindentation process.[66–71] We followed a protocol detailed in Refs.[70,71] for the prediction of the Young's modulus of single-layer and multi-layer graphene. Within these calculations, we modeled the indenter tip as a $a = 2$ nm diameter diamond nanosphere comprising 779 carbon atoms. The nanosphere was initially placed at $z = +2$ nm above the center of the relaxed nanosheet lying in the xy plane and then driven into the sheet at a with 0.002 nm/ps pulling rate and (-1000) kJ/(mol.nm^2) elastic constant towards corresponding points below sheets using center-of-mass pulling over the course of a 2 ns simulation (Fig. 2b, left). A 1.5 nm strip around the perimeter of the (14.2 × 14.2) nm^2 nanosheet was held fixed by freezing all atoms within this clamping zone. We tracked the z-component of the loading force F_z experienced by the nanosheet over the course of the simulation together with the z-component of the displacement of the nanosheet δ_z and fitted the initial regime of the F_z–δ_z force-indentation curve using a Hertz model $F_z = \frac{4Y\sqrt{R}}{3(1-\nu^2)}\delta_z^{3/2}$, where Y is the Young's modulus, ν is the Poisson ratio, and R is the radius of the parabolic tip (Fig. 2b, right) [72,73] The diamond nanosphere employed here possesses $R = 1$ nm, and we adopt a Poisson modulus of $\nu = 0.3$ based on experimental measurements of polymeric materials.[74] A number of possible contact mechanics models are available to fit the simulated nanoindentation data,[72,75] but the spherical nanoindenter Hertz model is used to mimic the analysis performed of our experimental data and, as we shall demonstrate, yields Young's moduli predictions in good agreement with our experimental measurements. Defining $(x, y) = (0, 0)$ as the center of the nanosheet, we repeated these calculations at a total of nine locations – $[(0, 0), (-0.5, -0.5), (-0.5, +0.5), (+0.5, -0.5), (+0.5, +0.5), (-1, -1), (-1, +1), (+1, -1), (+1, +1)]$ nm – to compute a mean Y and estimate its standard error. Additionally, as an internal consistency check that the size of the nanosheet was sufficiently large to avoid finite size effects, we verified that the moduli computed over the four $(\pm 0.5, \pm 0.5)$ nm calculations and over the four $(\pm 1, \pm 1)$ nm calculations lay within standard errors of one another.

Computational prediction of nanosheet bending moduli by uniaxial deformation. Directional bending moduli Y_α in the two dimensions $\alpha = \{x{,}y\}$ of the peptoid nanosheets were calculated using uniaxial deformation simulations. Given the crystal nature of the peptoid nanosheets, we follow the approach detailed in Ref.[76] that is appropriate for crystalline systems and which estimates the bending modulus as the slope of the initial linear region of the stress-strain response curve. Approaches more suitable for fluid/gel membranes rely on inducing buckling of the sheet and fitting of a more complicated functional form.[77–79] Calculations were conducted on initially relaxed nanosheets in the semi-isotropic NPT ensemble at 300 K and 1 bar employing a Nosé-Hoover thermostat[60] with a time constant of 1.0 ps and Parrinello-Rahman barostat[61] with a time constant of 1.0 ps and compressibility of 4.5×10^{-5} bar^{-1} for the z dimension and 0 bar^{-1} for xy dimensions since we do not couple the plane undergoing deformation. To estimate the bending modulus Y_α, we applied a constant deformation rate of (-1×10^{-5}) nm/ps to the α-dimension of the cubic simulation box over the course of a 300 ns production run (Fig. 3a). The instantaneous strain at any instant t is defined as $\gamma_\alpha(t) = [L_\alpha(t) - L_\alpha(0)] / L_\alpha(0)$, where $L_\alpha(t)$ is the simulation box side length in the α dimension at time t. The corresponding instantaneous stress $\tau_\alpha(t)$ in the α-dimension is computed from the $P_{\alpha\alpha}(t)$ component of the stress tensor computed using the `gmx energy` implementation within Gromacs 2019.2.[56,57] The directional bending modulus Y_α is estimated as the slope of the τ_α-γ_α stress-strain curve within the linear response regime (Fig. 3b). Calculations in x and y were performed for Nbrpm6Nc6 and NbrpeNbrpm3Nc6, and Nbrpe6Nc6 nanosheets in both parallel V and anti-parallel V configurations. Four independent simulations were conducted for each system to compute means and estimate standard errors for a total of 48 simulations.

3 Results and Discussion

3.1 Experimental measurement and computational prediction of Young's moduli of peptoid nanosheets

It has been proposed that peptoid nanotubes assembled from amphiphilic diblocks form through a putative sheet-to-tube transition by rolling up the nanosheet.[38] The mechanical resistance to this rolling transition is governed by the bending modulus. Here, we measured the effective Young's modulus of Nbrpe6Nc6 and (NbrpeNbrpm)3Nc6 nanosheets using AFM-based nanoindentation readings taken over a grid of 512×512 = 262,144 locations over the nanosheet (Fig. 2a). We also conducted virtual nanoindentation calculations using all-atom molecular dynamics simulations (Fig. 2b). The purpose of the calculations was twofold: to validate the molecular models by testing their capability to predict an experimentally measurable materials property, and to permit the estimation of the Young's modulus of Nbrpm6Nc6 nanosheets, which – as a tube-forming sequence – are not readily accessible to experimental measurements but can be computationally constructed and their materials properties calculated. We present in Fig. 2c the results of our experiments and computations from which we make four primary observations.

First, we see good agreement between the computational predictions and experimental measurements. The experimental Young's moduli for Nbrpe6Nc6 and (NbrpeNbrpm)3Nc6 are in quite good agreement with the computational predictions: Nbrpe6Nc6: (1.20±0.41) GPa (expt), (0.77±0.12) GPa (comput, parallel V), (1.00±0.06) GPa (comput, anti-parallel

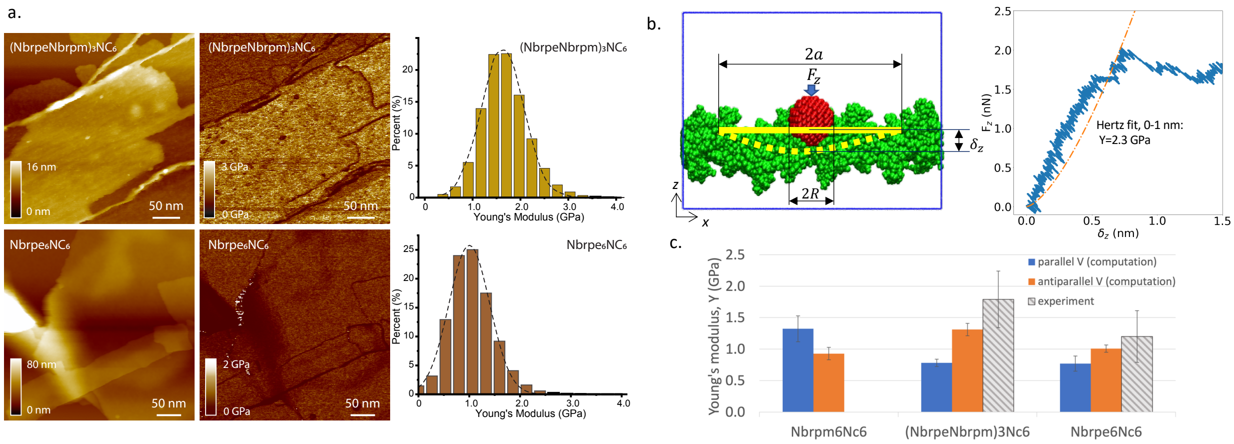

Figure 2: Experimental measurement and computational prediction of nanosheet Young's moduli by nanoindentation. (a) Experimental AFM measurement of Nbrpe6Nc6 and NbrpeNbrpm3Nc6 nanosheets showing (left) AFM height images of peptoid nanosheets, (middle) simultaneously resolved maps of the experimentally measured Young's modulus over the nanosheets, and (right) distributions of moduli. (b) Illustration of the force-indentation response extracted from molecular dynamics simulations of the simulated nanoindentation procedure applied to the parallel V (NbrpeNbrpm)3Nc6 nanosheet. A diamond nanosphere is driven at constant velocity v_z to perpendicularly impinge into the xy plane of the relaxed peptoid nanosheet. The force-indentation F_z-δ_z response is recorded over the course of the simulation and fitted to a Hertz model within the small indentation regime to infer the Young's modulus Y. (c) Experimental AFM measurement and computational prediction of Young's moduli for Nbrpm6Nc6, (NbrpeNbrpm)3Nc6, and Nbrpe6Nc6 nanosheets. Computational error bars correspond to standard errors computed over nine independent measurements at different indentation locations. Experimental error bars correspond to standard errors over the 512×512 = 262,144 measurement locations. Since Nbrpm6Nc6 spontaneously assembles into nanotubes, nanosheets are not available for experimental measurements but can be computationally constructed and interrogated for their materials properties.

V); (NbrpeNbrpm)3Nc6: (1.79±0.45) GPa (expt), (0.78±0.06) GPa (comput, parallel V), (1.31±0.10) GPa (comput, anti-parallel V). Specifically, for Nbrpe6Nc6 the experimental measurements and computational predictions for both the parallel and anti-parallel sheets lie within error bars, and for (NbrpeNbrpm)3Nc6 the experimental measurement and anti-parallel computational prediction agree within error bars. This provides good validation of the predictive capacity of the computational models and lends credence to our computational predictions of the Young's modulus for Nbrpm6Nc6 – Nbrpm6Nc6: (1.32±0.21) GPa (comput - parallel V), (0.93±0.10) GPa (comput - anti-parallel V) – for which experimental measurements are unavailable.

Second, the predicted Young's moduli predictions for the parallel V and anti-parallel V configurations are, within error bars, relatively close for the three systems, differing by less than 0.37 GPa. Prior free energy calculations have predicted the parallel V and anti-parallel V morphologies to be equally thermodynamically stable and have suggested that nanosheets may actually exist as a mix of the two morphologies.[41] The similarity of the parallel V and anti-parallel V moduli is consistent with a picture of similar thermodynamic and mechanical stability and a possible mixed character of the nanosheets.

Third, we see no correlation, at least within the resolution of our measurements and predictions, between the Young's modulus and the propensity of a peptoid sequence to preferentially assemble into nanotubes (Nbrpm6Nc6), nanosheets (Nbrpe6Nc6), or aggregates of mixed character ((NbrpeNbrpm)3Nc6), with all three sequences forming peptoid nanosheets with Young's moduli of approximately 1 GPa.

Fourth, we observe that the experimentally measured Young's moduli of ∼1-2 GPa for the (NbrpeNbrpm)3Nc6 and Nbrpe6Nc6 peptoid nanosheets is approximately one order of magnitude smaller than the values of ∼13-17 GPa measured for the closely related Nce6Nbrpm5, Nce6Nbrpm6, and Nce6Nbrpm7 nanotubes previously reported by Jin et al.[38] The measurements conducted herein used an AFM tip to measure the force-indentation response of a flat nanosheet, whereas those conducted by Jin et al. used an AFM tip to deform an entire self-assembled nanotube from a circular to elliptical cross-sectional geometry. Accordingly, whereas the present measurements consider only the intrinsic properties of a flat nanosheet, the prior measurements reflect the global elastic response of the nanotube as a function of both the intrinsic materials properties of the tube wall and the influence of the self-assembled cylindrical geometry.

3.2 Computational prediction of bending moduli of peptoid nanosheets

We have previously proposed a putative sheet-to-tube transition in which peptoid nanotubes are formed by rolling up peptoid nanosheets along their x-axis[38] (Fig. 1d). However, the rationale for tube rolling along the x-direction as opposed to the y-direction has not previously been supported. Heartened by the good experimental agreement of the Young's modulus predictions from our computational model, we use our model to predict the axially-resolved bending moduli Y_x and Y_y along the two axes of the planar nanosheet by computing the slope of the initial linear region of the stress-strain response under uniaxial deformation (Fig. 3a,b). We present the results of our calculations in Fig. 3c.

With the exception of the parallel V Nbrpm6Nc6 system, we predict the y-bending modulus Y_y corresponding to deformation of the nanosheets along the pi-stacked crystalline peptoid columns to lie in the approximate range of 1.2-1.5 GPa for both the parallel V and anti-parallel V arrangements for all three peptoid sequences. We predict the x-bending modulus Y_x corresponding to bending of the nanosheets across the pi-stacked peptoid columns to be substantially lower, with these values lying in the approximate range 0.1-0.6 GPa. These results suggest that bending deformation of the nanosheets is generally easier along the x-axis in which the pi-stacked columns interdigitate via their side chains compared to the y-axis in which the columns form by pi-stacking of the side chain aromatic rings. This is consistent with intuition that it should require more force to disrupt the columnar crystals formed by pi-stacking of multiple aromatic side chains in y compared to deformation of the relatively weaker interactions due to interdigitation of the side chains that do not involve pi-stacking in x. This determination is consistent with the previously proposed model in which the nanotube structure corresponds to rolling up a nanosheet in the x-dimension such that the columnar pi-stacked crystals are aligned along the axis of the tube.[38]

The small y-bending modulus recorded for the parallel V Nbrpm6Nc6 nanosheet is both anomalous relative to the other sequences and highly reproducible, with our four independent calculations returning values of Y_y within the range 0.2-0.7 GPa. To probe the origin of this behavior we analyzed the packing of the peptoids within the sheets under the application of an applied deformation. In Fig. 3d we present snapshots of parallel V Nbrpe6Nc6, (NbrpeNbrpm)3Nc6, and Nbrpm6Nc6 sheets in the undeformed (i.e., γ_y=0) state and under

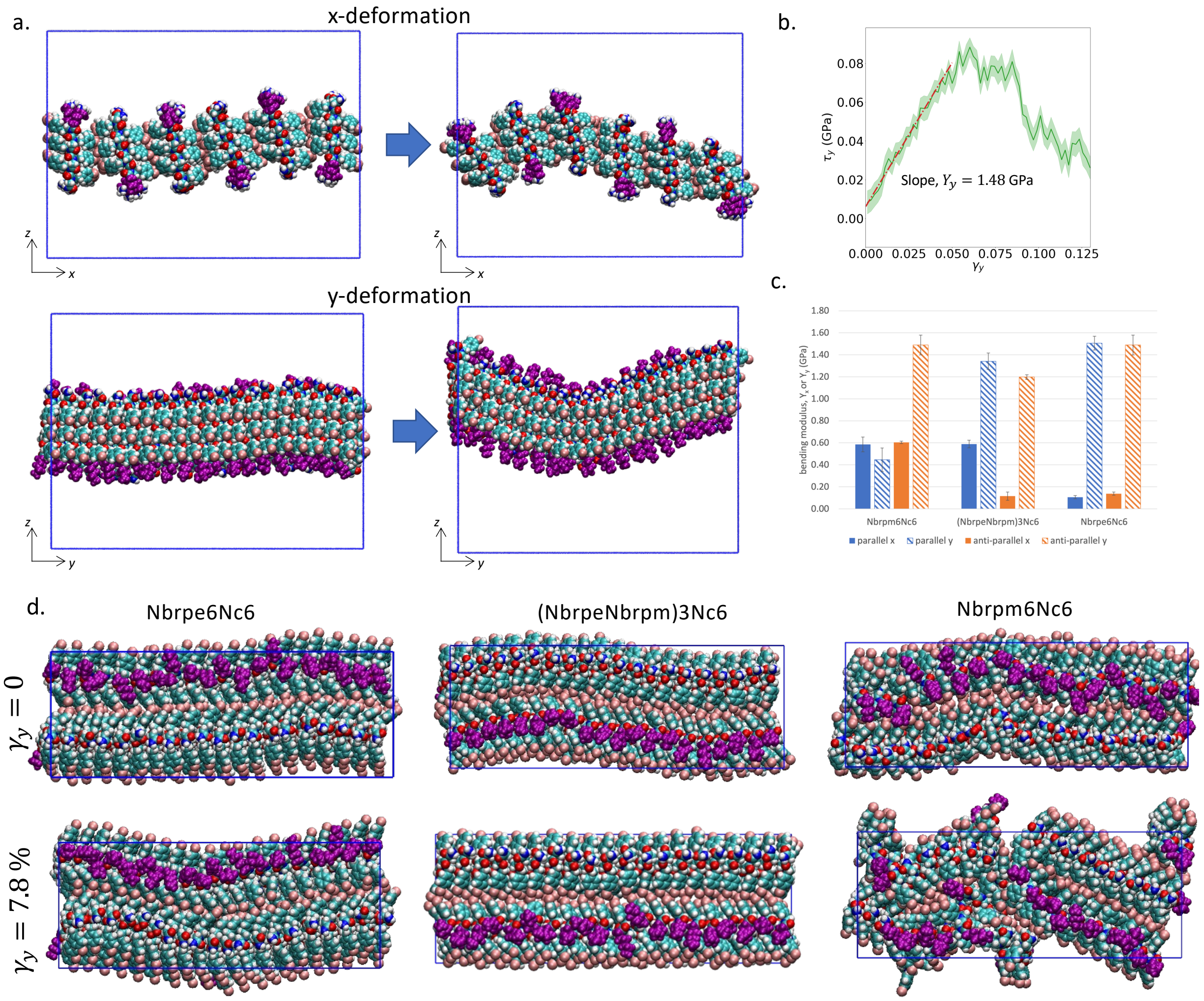

Figure 3: Computational prediction of nanosheet directional bending moduli by uniaxial deformation. (a) Application of uniaxial deformation in x (upper) and y (lower) directions induce the nanosheet to bend along these axial directions. We illustrate here as an example the initial and final states of a Nbrpe6Nc6 nanosheet in a parallel V orientation. (b) Illustration of the stress-strain curve τ_y-γ_y for the y-bending calculation presented in panel a. The bending modulus is estimated as the slope of a least-squares linear fit to the low-stress/low-strain linear response regime. (c) Directional bending moduli in x and y for parallel V and anti-parallel V nanosheets. Error bars correspond to standard errors estimated over four independent calculations. (d) Comparison of parallel V Nbrpe6Nc6, (NbrpeNbrpm)3Nc6, and Nbrpm6Nc6 sheets in the undeformed (i.e., γ_y=0) state and under the application of a γ_y=7.8% y-strain. The Nbrpm6Nc6 sheet exhibits substantially more disorder and loss of alignment between peptoid monomers, suggesting a possible structural origin for the anomalously low y-bending modulus Y_y of the parallel V Nbrpm6Nc6 sheet relative to the parallel V Nbrpe6Nc6 and parallel V (NbrpeNbrpm)3Nc6 sheets.

the application of a γ_y=7.8% y-strain. Comparing the strained configurations, we visually observe that the parallel V Nbrpm6Nc6 sheet exhibits substantially more disorder and loss of alignment between peptoid monomers constituting the sheet compared to the parallel V Nbrpe6Nc6 and parallel V (NbrpeNbrpm)3Nc6 sheets. This loss of order suggests a possible structural origin for the anomalously low y-bending modulus Y_y of the parallel V Nbrpm6Nc6 sheet relative to the other two sequences, although further study, additional simulations, and quantitative analysis of the change in structural packing along the deformation pathway would be required to fully resolve the precise inter-molecular interactions and structural changes underpinning this behavior. This result suggests that it may be equally easy to bend a parallel V Nbrpm6Nc6 nanosheet in x and y, such that we might anticipate these nanotubes to be a mixture of these geometries. However, previous calculations have identified the parallel V and anti-parallel V morphologies to be equally thermodynamically stable, suggesting that nanosheets may comprise a mixture of these two structures.[41] It is anticipated that the much larger Y_y value for the anti-parallel V components of the sheet would resist bending in y and make bending in x net more favorable overall.

3.3 Molecular structure of Nbrpm6Nc6 peptoid nanotubes.

Our axially-resolved bending modulus calculations support our previously proposed model of a peptoid nanotube as a nanosheet rolled up along its x-direction,[38] but it is not known whether the structure of the peptoid monomers and packing of their side chains within the nanotube follow the same arrangement as those within the nanosheet. To probe the structure of the nanotube walls, we constructed an initial Nbrpm6Nc6 nanotube by extracting a two-column unit cell from a relaxed Nbrpm6Nc6 nanosheet and assembling it into a cylindrical cross-section of radius R that was subjected to multiple cycles of gentle heating and structural relaxation. Terminal nanotubes comprising 76 columnar peptoid stacks and a corresponding radius of $R \approx 17$ nm in both parallel V and anti-parallel V arrangements are presented in Fig. 4a,b as a representative illustration. We observe that the molecular organization of the nanotube walls remain similar to that within the nanosheet with subtle, but significant, differences. In both cases we observe a tilt in pi-stacked crystalline columns relative to the radial vector emanating from the nanotube center and an offset in the packing of the interdigitated side chains. In the parallel V case, the tilt angles lie in the range 0-30° with a mean of $\sim$5°, whereas in the anti-parallel case they lie in the range 0-40° with a mean of $\sim$20°. A t-test reveals that we can reject the null hypothesis that the distribution of tilt angles in the two cases are drawn from the same distribution at a significance level of α=0.01. The origin of this difference in terms of the precise intermolecular interactions and packing differences in the two configurations at this stage remains elusive and would require additional more detailed simulations and free energy calculations to map out the structural changes and associated free energy landscape as a function of tilt angle. We constructed models of nanotubes comprising n = [64, 68, 72, 76, 80, 84, 88] columnar peptoid stacks within their circumference that resulted in nanotubes with observed radii R = [15.00±4.25, 15.62±2.69, 16.24±2.32, 17.11±2.05, 18.46±3.84, 19.03±2.48, 20.00±2.66] nm centered around the experimentally reported characteristic radius of $\sim$19 nm for the closely related Nbrpm6Nce6 peptoid sequence[38](Fig. 4c, left). The fluctuations in the tube radius σ_R are a function of R that exhibits a minimum at a radius of approximately $R = 17$ nm for both the parallel V and anti-parallel V morphologies (Fig. 4c, right). This suggests that there may be a most stable radius of the nanotube at which fluctuations are minimized.

3.4 Theoretical model of nanotube stability

To provide molecular understanding of the sharp distribution of Nbrpm6Nc6 nanotube radii observed in experiment[38] and our simulation prediction of a nanotube radius at which fluctuations are minimized, we constructed a thermodynamic model of nanotube stability employing simple continuum mechanics.

Model development. Building upon a free energy model for the stability of carbon nanotubes,[80,81] we define the free energy of a cylindrical nanotube of radius R and length

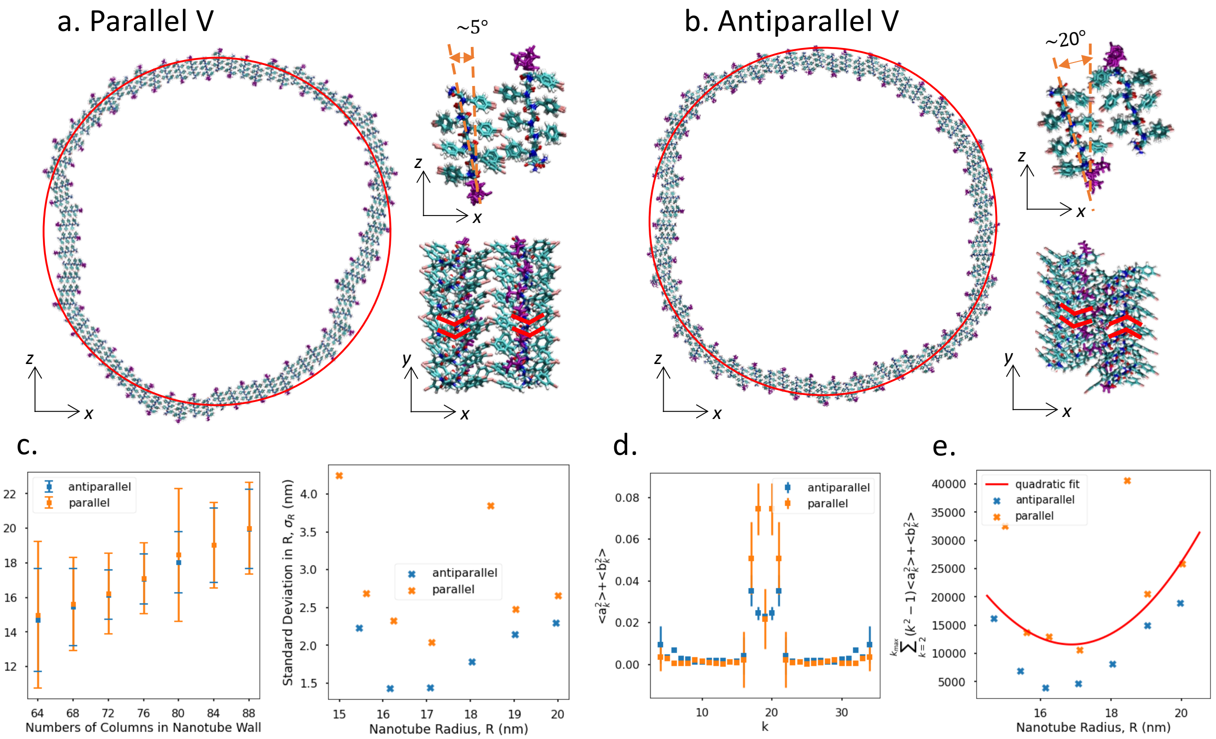

Figure 4: Molecular model of Nbrpm6Nc6 nanotubes. Computational construction and relaxation of molecular models of Nbrpm6Nc6 nanotubes constructed from 76 columnar peptoid stacks in the (a) parallel V and (b) anti-parallel V orientations. We present a zoomed in view of the two-column unit cell of the nanotube wall comprising two y-stacked columns lying along the long axis of the nanotube. Iterative relaxation of the unit cell and cylindrical cross-section converges to a structure in which the y-stacked columns are tilted relative to the radial vector illustrated by the red arrow and possess an offset in the interdigitated packing of side chains between adjacent columns in the nanotube wall. In the parallel V case, the mean tilt angle is $\sim 5°$ and in the anti-parallel case is $\sim 20°$. The distribution of tilt angles in the parallel V and anti-parallel V cases are statistically distinguishable as confirmed by a t-test. (c) The left-hand plot illustrates the relationship between number of columns constituting the nanotube wall and the radius R of the nanotube measured by fitting a circle to the tube cross-section over the course of the molecular simulation. Error bars show σ_R corresponding to the standard deviations of R over the course of the simulation that reflect the magnitude of the fluctuations in the radius of the nanotube. The right-hand plot illustrates the relationship between σ_R and R to show that the fluctuations are minimized at approximately $R = 17$ nm for both the parallel and anti-parallel geometries. (d) Time averaged squared Fourier coefficients $\langle a_k^2 \rangle + \langle b_k^2 \rangle$ as a function of wavenumber k computed over the 10 ns simulation trajectories of the terminal relaxed nanotubes illustrated for the 76 column nanotube with corresponding radius of $R \approx 17$ nm. Data are reported up to a maximum wavenumber of $k_{\max} = 45$ beyond which the coefficient magnitudes are approximately zero. Standard errors in the time averages are estimated by five-fold block averaging. (e) Estimated contribution of capillary wave term to the wall area-normalized free energy $\sum_{k=2}^{k_{\max}}(k^2-1)(\langle a_k^2 \rangle + \langle b_k^2 \rangle)$ (cf. Eqn. 11) as a function of tube radius R and the corresponding least-squares quadratic fit.

L_t relative to its constitutive isolated monomers,

$$F_{\text{total}} = F_{\text{bend}} + F_{\text{assoc}} + F_{\text{capillary}}, \tag{1}$$

where F_{bend} is the contribution due to the bending strain energy required to roll the nanosheet into a nanotube, F_{assoc} is the favorable free energy of association of the monomers comprising the nanotube, and $F_{\text{capillary}}$ is the interfacial free energy associated with the interface between the tube and the solvent. We assume that the nanotube wall is incompressible so that there are no contributions to the free energy associated with compression tangential to the tube wall and that the cross-sectional area of the tube is conserved.

Assuming an elastic continuum, the bending free energy can be expressed as $F_{\text{bend}} = L_t B/2 \oint (1/\rho^2) dl$, where L_t is the axial length of the cylindrical tube, B is the bending stiffness, ρ is the local radius of curvature, and $P = \oint dl$ is a curvilinear integral defining the perimeter of the nanotube cross-section. The association free energy can be expressed as $F_{\text{assoc}} = -\epsilon(P/\delta)L_t$ where δ is the width of a column of peptoid monomers within the nanotube perimeter, (P/δ) is the number of monomer columns comprising the perimeter, and we define ϵ as a non-negative constant specifying the favorable free energy of association between adjacent pairs of monomers within the tube wall per unit axial length of the tube. Monomer association is driven largely by the hydrophobic effect which makes monomer association thermodynamically spontaneous.[41] We assume that ϵ is independent of the nanotube radius R. The capillary, or interfacial, free energy is given by $F_{\text{capillary}} = L_t \sigma \oint dl$, where σ is the surface tension between the nanotube wall and the solvent. Inserting these expressions into Eqn. 1 and assuming a uniform axial cross section, we divide through by L_t to obtain the free energy per unit axial length,

$$\frac{F_{\text{total}}}{L_t} = \frac{B}{2} \oint \frac{1}{\rho^2} dl - \frac{\epsilon P}{\delta} + \sigma \oint dl. \tag{2}$$

The peptoid nanotube is a supramolecular object that may change its radius by association or dissociation of peptoid monomers. Thermodynamically, the relevant free energy to minimize is the per monomer free energy. As such, we divide through by the number of monomer columns comprising the nanotube perimeter (P/δ) where $P = 2\pi R$ is the equilibrium perimeter of the cylindrical cross-section of the tube to obtain an expression for the free energy per peptoid monomer within the cylindrical cross-section,

$$f_{\text{total}} = \frac{F_{\text{total}}}{L_t(2\pi R/\delta)} = \frac{\delta B}{4\pi R}\oint \frac{1}{\rho^2}dl - \epsilon + \frac{\delta\sigma}{2\pi R}\oint dl. \tag{3}$$

To make progress, we now develop an expression for the location of the perimeter of the tube cross section as a Fourier expansion in polar coordinates,[82,83]

$$r(\phi) = R\left[1 + a_0 + \sum_{k=1}^{\infty} a_k \cos(k\phi) + \sum_{k=1}^{\infty} b_k \sin(k\phi)\right], \tag{4}$$

where a_k and b_k are Fourier coefficients defined as,

$$a_k = \frac{1}{\pi R}\int_0^{2\pi} r(\phi)\cos(k\phi)\ d\phi, \tag{5}$$

$$b_k = \frac{1}{\pi R}\int_0^{2\pi} r(\phi)\sin(k\phi)\ d\phi. \tag{6}$$

Physically, Eqn. 4 allows for the possibility of thermally-driven capillary waves and represents the location of the fluctuating interface relative to the equilibrium circular cross-section of radius R through an angular dependence of the tube radius.[82,83] The value of a_0 is specified by the incompressibility condition wherein the enclosed equilibrium cross-sectional area $A_x = \pi R^2$ is conserved under deformation of the interface,[82,83]

$$A_x = \frac{1}{2}\int_0^{2\pi} r^2(\phi)\ d\phi = \pi R^2\left[1 + 2a_0 + \frac{1}{2}\sum_{k=1}^{\infty} a_k^2 + \frac{1}{2}\sum_{k=1}^{\infty} b_k^2\right] = \pi R^2,$$

$$\Rightarrow a_0 = -\frac{1}{4}\sum_{k=1}^{\infty}(a_k^2 + b_k^2), \tag{7}$$

such that Eqn. 4 becomes,

$$r(\phi) = R\left[1 - \frac{1}{4}\sum_{k=1}^{\infty}(a_k^2 + b_k^2) + \sum_{k=1}^{\infty} a_k \cos(k\phi) + \sum_{k=1}^{\infty} b_k \sin(k\phi)\right]. \tag{8}$$

Next, we compute the circumference of the cylindrical nanotube cross-section by performing the curvilinear integral $\oint dl$ that appears in the capillary contribution to the free energy by employing the Monge representation of the circumferential contour in the small fluctuation limit and inserting Eqn. 8,[82,83]

$$\begin{aligned}\oint dl &= \int_0^{2\pi} \sqrt{\left(r^2(\phi) + \left(\frac{\partial r(\phi)}{\partial \phi}\right)^2\right)}\, d\phi \\ &\approx \int_0^{2\pi} r(\phi)\, d\phi + \frac{1}{2R}\int_0^{2\pi}\left(\frac{\partial r(\phi)}{\partial \phi}\right)^2 d\phi \\ &= 2\pi R + \frac{\pi R}{2}\sum_{k=2}^{\infty}(k^2-1)(a_k^2 + b_k^2). \end{aligned} \tag{9}$$

In the absence of any capillary wave fluctuations (i.e., $a_k = b_k = 0,\ \forall k$) we recover the equilibrium result for a static circular cross-section $P = 2\pi R$.

Now, returning to our expression for the per peptoid free energy in Eqn. 3, we insert Eqn. 9 into the capillary (i.e., third) term to model contributions resulting from both the equilibrium circular cross-section and capillary wave fluctuations. For the bending (i.e., first) term, we make the simplifying assumption that the effect of the capillary waves upon the local curvature and the bending energy can be neglected. This is valid in the limit of small magnitude fluctuations and allows us to take the $1/\rho^2$ out of the integral, set $\rho = R$, and replace the remaining integral as $\oint dl = 2\pi R$. This results in our final expression for the free energy per peptoid monomer per unit axial length,

$$f_{\text{total}}(R) = \frac{\delta B}{2R^2} - \epsilon + \delta\sigma + \frac{\delta\sigma}{4}\sum_{k=2}^{\infty}(k^2-1)(a_k^2(R) + b_k^2(R)), \tag{10}$$

where we identify the first term as the bending contribution, the second as the contribution from hydrophobic monomer association, the third as the equilibrium interfacial contribution for a static cylindrical nanotube, and the fourth as the contribution due to the thermally-driven capillary wave spectrum in the tube wall. We have also made explicit the dependence of the overall free energy and the capillary wave Fourier coefficients on the tube radius.

Model analysis. This expression in Eqn. 10 is extremely informative in encapsulating our physical understanding of the various free energy contributions into a mathematical expression. Identifying B, ϵ, σ, a_k, and b_k as non-negative materials properties or Fourier coefficients, we see that the bending term favors tubes of infinite radius (i.e., sheets) to minimize the free energy cost associated with bending deformation. The association free energy term is independent of tube radius R since, under the assumption that the association free energy between peptoid monomers does not vary with their angle of contact within the tube wall, every column of peptoid monomers in the tube wall possesses exactly two neighboring columns regardless of tube radius. The static capillary/interfacial term is also independent of R since, under the incompressibility assumption, the total peptoid surface area exposed to solvent does not depend on the geometry of the tubes and sheets within which the peptoids are assembled. The capillary wave contributions lead to an increase in the tube free energy associated with axially-symmetric capillary excitations in the tube wall that elevate the tube free energy. The dependence of the magnitude of these excitations (i.e., a_k and b_k) is dictated by both the tube radius and molecular details of the system including the structural packing of the monomers within the tube wall, solvent interaction, and temperature, and must generally be empirically determined by numerical simulation or experimental observations.[82]

Predicted tube radius. To simplify our analysis of the optimal nanotube radius, we discard the terms with no R dependence in Eqn. 10 by redefining the arbitrary zero of the free energy per peptoid monomer per unit axial length and also dividing through by the peptoid monomer width δ,

$$\tilde{f}_{\mathrm{total}}(R) = \frac{f_{\mathrm{total}}(R) + \epsilon - \delta\sigma}{\delta} = \frac{B}{2R^2} + \frac{\sigma}{4}\sum_{k=2}^{\infty}(k^2 - 1)(a_k^2(R) + b_k^2(R)). \tag{11}$$

Determination of the optimal nanotube radius amounts to minimizing the sum of the bending and capillary wave terms in Eqn. 11.

We can obtain an analytical estimate for the bending term by appealing to the materials properties of the peptoid nanotube. The bending stiffness can be expressed as $B = Yh^3/12(1-\nu^2)$, where Y is the Young's modulus, h is the tube thickness, and ν is the Poisson ratio.[80,81] Following our experimental measurements and computational predictions of the Young's moduli for these peptoid nanosheets, we adopt a characteristic value of $Y = 1$ GPa (Fig. 2c). The wall thickness of the nanotubes is approximately equal to the fully extended length of a single peptoid chain for which we adopt a characteristic value of $h = 2.8$ nm. The Poisson ratio for this specific peptoid material is unknown, but here we adopt a characteristic Poisson ratio of polymeric materials $\nu = 0.3$.[74] This results in a bending stiffness of approximately $B = 1.2$ MJ/mol.

The absence of a good analytical model for the Fourier coefficients $a_k(R)$ and $b_k(R)$ as a function of tube radius means that we cannot conduct a simple minimization of Eqn. 11 in the presence of the capillary wave term. We can, however, turn to our numerical simulations of relaxed Nbrpm6Nc6 nanotubes of various radii in the range $R = 15$-20 nm. We already observed the fluctuations in the tube wall to be strongly dependent on the tube radius and that the fluctuation magnitude exhibited a minimum at an intermediate radius of $R \approx 17$ nm (Fig. 4c). Motivated by our theoretical model, we conducted a Fourier analysis of the fluctuation spectrum by applying fast Fourier transforms (FFT) to the contours of the cross-sectional perimeter of the tube wall $r(\phi)$ harvested over the course of our 10 ns simulation trajectories of the terminal relaxed nanotubes.[82,84] We report the time-averaged sum of the Fourier coefficients $\langle a_k^2 \rangle + \langle b_k^2 \rangle$ as a function of the wavenumber k for each tube radius R

(Fig. 4d) and the aggregated contribution $\sum_{k=2}^{\infty}(k^2-1)(\langle a_k^2\rangle + \langle b_k^2\rangle)$ of the capillary wave term to the wall area-normalized free energy in Eqn. 11 as a function of tube radius R (Fig. 4e). These plots illustrate that tubes of different radii support quite different capillary wave spectra and therefore different contributions to the nanotube free energy.

Following Eqn. 11, in Fig. 5 we plot $\tilde{f}_{\text{bend}} = B/2R^2$, $\tilde{f}_{\text{capillary}} = \frac{\sigma}{4}\sum_{k=2}^{\infty}(k^2-1)(a_k^2(R) + b_k^2(R))$, and $\tilde{f}_{\text{total}} = \tilde{f}_{\text{bend}} + \tilde{f}_{\text{capillary}}$. The bending term is computed analytically and decreases monotonically as the square of the tube radius. The capillary term is computed by adopting a characteristic value for the surface tension of $\sigma = 30$ mN/m[85,86] and making a least squares quadratic fit to our molecular simulation data collected for parallel V and anti-parallel V tubes of radius R = 15-20 nm. An Akaike information criterion (AIC) analysis reveals a quadratic fit to be the simplest model best supported by the data.[87] For reference we also plot the raw data for the capillary contributions $\frac{\sigma}{4}\sum_{k=2}^{\infty}(k^2-1)(a_k^2(R) + b_k^2(R))$ collected from our parallel V and anti-parallel V simulations assuming a surface tension of $\sigma = 30$ mN/m. The capillary contribution data is rather noisy but does exhibit a non-monotonic trend, with our fit predicting a minimum at $R \approx 17$ nm in good accord with the minimum in the magnitude of the tube wall fluctuations (Fig. 4c). For the present choice of model parameters, the bending contribution $\tilde{f}_{\text{bend}}$ (red dotted line) is approximately five orders of magnitude smaller than the capillary contribution $\tilde{f}_{\text{capillary}}$ (thick blue solid line), meaning that the bending contribution to the free energy can be neglected. As such, the capillary term governs the system thermodynamics and $\tilde{f}_{\text{total}}$ (black dot-dashed line) is indistinguishable from $\tilde{f}_{\text{capillary}}$ (thick blue solid line). The minimum in $\tilde{f}_{\text{total}}$ therefore also lies at $R \approx 17$ nm and can be understood intuitively as the radius at which the contribution of these capillary fluctuations to the free energy are minimized.

The simple nature of our theoretical model means that we should not expect quantitative agreement with experimental observations, but the predicted optimal ∼17 nm tube radius is in remarkably good accord with the characteristic ∼20 nm radius observed for the Nbrpm6Nc6 nanotubes in the present work (Fig. 1b) and the characteristic ∼19 nm

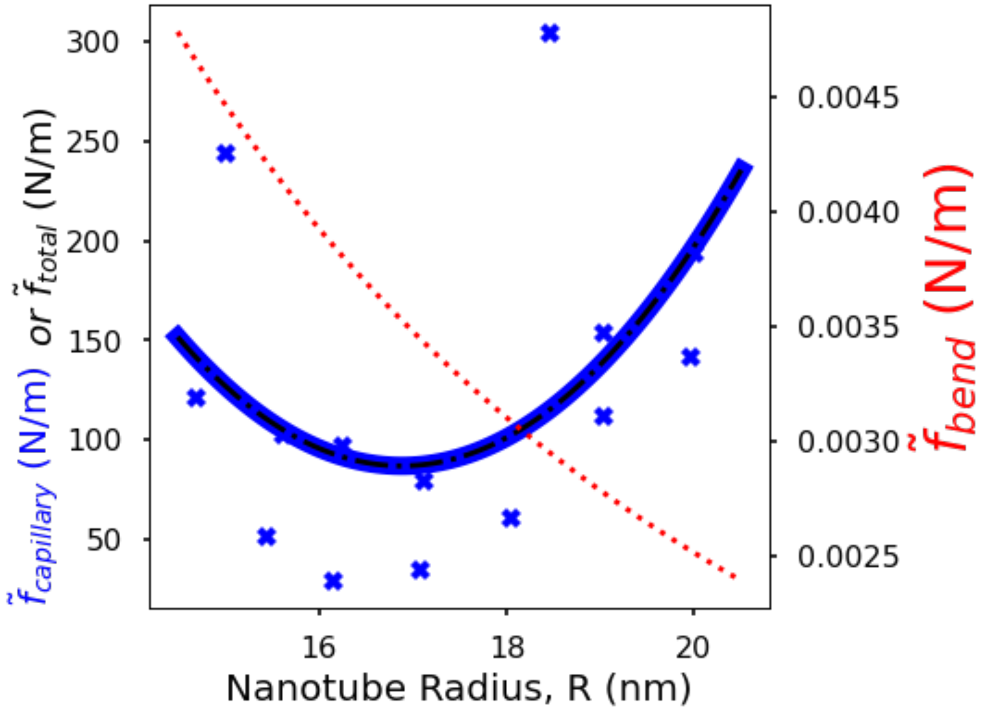

Figure 5: Predicted per monomer nanotube free energy as a function of tube radius. The total free energy $\tilde{f}_{\text{total}}$ is the sum of the bending $\tilde{f}_{\text{bend}} = B/2R^2$ (red dotted line) and capillary $\tilde{f}_{\text{capillary}} = \frac{\sigma}{4}\sum_{k=2}^{\infty}(k^2-1)(a_k^2(R)+b_k^2(R))$ (thick blue solid line) contributions. $\tilde{f}_{\text{bend}}$ is estimated analytically from estimation of B and is a monotonically decreasing function of R. $\tilde{f}_{\text{capillary}}$ is estimated numerically from a least squares quadratic fit to data points $\frac{\sigma}{4}\sum_{k=2}^{\infty}(k^2-1)(a_k^2(R)+b_k^2(R))$ collected from MD simulations of parallel V and anti-parallel V nanotubes with radii R = 15-20 nm and assuming a surface tension of σ = 30 mN/m (blue crosses). The bending contribution to the free energy is approximately five orders of magnitude smaller than the capillary contribution, meaning that the former can be effectively neglected and the sum of the two contributions $\tilde{f}_{\text{total}} = \tilde{f}_{\text{bend}} + \tilde{f}_{\text{capillary}}$ (black dot-dashed line) is indistinguishable from $\tilde{f}_{\text{capillary}}$ (thick blue solid line) and possesses a predicted free energy minimum at $R \approx 17$ nm.

radius for the closely related Nbrpm6Nce6 nanotubes reported by Jin et al.[38] Within the theoretical model, the independence of the hydrophobic association free energy follows from the assumption that each column of peptoid monomers within the tube wall contacts precisely two neighboring peptoid columns and that the association free energy between peptoid columns is not a function of their intermolecular contact angle. The independence of the static capillary/interfacial terms with respect to tube radius follows from the incompressibility assumption wherein the cross-sectional area is conserved under deformation of the interface. Perhaps the most meaningful and insightful predictions of the model are (i) the small magnitude of the bending contribution to the free energy, (ii) the primary control of tube stability by the capillary wave contributions, and (iii) the existence of a "Goldilocks" minimum in the capillary wave contributions at intermediate radii, wherein the free energy increases at both smaller radii – presumably due to increased capillary fluctuations associated with poorer side chain interdigitation and packing of the columnar peptoid stacks at high curvatures leading to structural instabilities – and larger radii – where the larger tubes support more and larger magnitude capillary fluctuations spanning a larger range of wavenumbers k. Empirically, we had numerical difficulty generating stable structures of Nbrpm6Nc6 nanotubes in our all-atom molecular simulations at radii much smaller than 15 nm and much larger than 20 nm. It is certainly possible that this was due, at least in part, to limitations in our nanotube construction protocol, but is consistent with the existence of a relatively narrow window of radii at which these nanotubes are structurally stable.

4 Conclusions

In this work, we employed all-atom molecular dynamics simulations and atomic force microscopy measurements to determine the mechanical properties of nanotubes and nanosheets assembled from Nbrpm6Nc6, (NbrpeNbrpm)3Nc6, and Nbrpe6Nc6 diblock amphiphilic peptoids, and related these properties to the structure and stability of the self-assembled morphologies. By bridging the microscopic mechanical properties to the mesoscopic supramolecular structure, this work offers new understanding and precepts for the engineering of peptoid nanomaterials with potential applications in biochemical and biomedical engineering. Experimental measurements of the Young's modulus of Nbrpe6Nc6 and (NbrpeNbrpm)3Nc6 nanosheets using AFM-based indentation are in good agreement with those predicted by our MD simulations in which we computationally simulate the indentation process. This agreement lends confidence to the computational methodology and supports the computational prediction of the Young's modulus for Nbrpm6Nc6 sheets, which, as a prototypical tube forming sequence, are not readily accessible for experimental interrogation. Additional MD simulations enable us to resolve the bending modulus along the two axes of the peptoid nanosheets, and resolve a typically lower modulus along the x-axis in which the peptoids stack by interdigitation of the side chains compared to the y-axis in which they form columnar crystals with pi-stacked side chains. This suggests that nanotubes are likely formed by rolling nanosheets along the axis of lower modulus, in agreement with a previously proposed molecular model.[38] Molecular modeling of nanotubes formed in this manner reveal subtle differences in the tilt and packing of side chains within the nanotube wall relative to their arrangement within nanosheets and, as such, the structure of a nanotube differs slightly from that expected by simply rolling up a nanosheet. MD simulations of nanotubes of varying radii formed by the tube-forming Nbrpm6Nc6 sequence suggest a stability optimum at a radius of ∼17 nm at which the fluctuations in the nanotube wall are minimized. We develop a simple thermodynamic model for the stability of peptoid nanotubes as a function of nanotube radius. The model predicts that nanotube stability is governed by contributions from bending strain associated with deforming a planar sheet into a tube and capillary wave fluctuations supported in the nanotube wall. For parameter choices appropriate to these peptoid systems, the bending contributions to the free energy are negligible compared to those from the capillary waves, and we predict an optimal nanotube radius of $R \approx 17$ nm where the capillary wave contributions to the free energy are minimized. This prediction is in remarkably good agreement with the ∼20 nm radius observed for the Nbrpm6Nc6 nanotubes in this work (Fig. 1b) and the characteristic ∼19 nm radius for the closely related Nbrpm6Nce6 nanotubes previously reported by Jin et al.[38]

A persistent puzzle in peptoid supramolecular assembly is the observation that subtle changes in the peptoid side chains can lead to the dramatic changes in the observed self-assembled morphology. For example, the elimination of a single C−C bond in the Nbrpe and Nbrpm side chains lead to Nbrpe6Nc6 peptoids forming nanosheets (Fig. 1a) whereas

Nbrpm6Nc6 peptoids form nanotubes (Fig. 1b). This work presents new understanding of the mechanical properties of peptoid nanosheets and nanotubes, their relationship to the observed self-assembled morphologies, and a numerical and theoretical rationalization for the tight nanotube radius distribution observed in experiments. The small magnitude of bending contributions to the nanotube free energy together with the similar Young's moduli for the sheet and tube-forming sequences studied here suggest that the bending modulus is, somewhat surprisingly, not the primary determinant of whether a particular peptoid sequence is likely to form a tube or a sheet. Viewing a sheet as a tube with infinite radius of curvature, our results instead suggest a more subtle dynamical mechanism wherein minimization of the capillary wave contributions to the free energy is the primary driver of adopting a tube (i.e., finite R) vs. sheet (i.e., infinite R) morphology. Consideration of a larger diversity of known tube and sheet-forming sequences would be required to further test this hypothesis, although computational challenges exist in simulating large diameter tubes and constructing stable and physically-meaningful hypothetical nanotubes from peptoid sequences known experimentally to only assemble into sheets. Should the model hold up to further scrutiny, it suggests that quantifying the capillary wave spectrum in molecular simulations may provide a route to make experimentally-testable predictions of whether a particular peptoid sequence is likely to assemble into a tube or a sheet. It also suggests a number of important additional questions that currently remain unanswered. What is the physicochemical origin of the differential capillary wave spectrum supported by supramolecular peptoid assemblies with subtly different side chains? Can the capillary wave spectrum be measured experimentally? What is the dynamical pathway and structural intermediates by which nanotubes form? Can the sheet/tube equilibrium by perturbed and/or controlled *in situ* by, for example, changing environmental conditions or stimuli responsive side chains? Can we prospectively mine chemical space for new putative tube and sheet forming sequences by high throughput virtual screening? Ultimately, we hope that these investigations and others will help establish a sequence-structure mapping wherein we can rationally design peptoid sequences to self-assemble nanoaggregates with engineered structure and properties.

Conflict of Interest Statement

A.L.F. is a co-founder and consultant of Evozyne, Inc. and a co-author of US Patent Applications 16/887,710 and 17/642,582, US Provisional Patent Applications 62/853,919, 62/900,420, 63/314,898, and 63/479,378 and International Patent Applications PCT/US2020/035206 and PCT/US2020/050466.

Acknowledgement

This material is based upon work supported by the US Department of Energy (DOE), Office of Science, Office of Basic Energy Sciences (BES), as part of the Energy Frontier Research Centers program: CSSAS – The Center for the Science of Synthesis Across Scales – under Award Number DE-SC0019288. AFM measurements were done at Pacific Northwest National Laboratory (PNNL). PNNL is operated by Battelle Memorial Institute for the US Department of Energy under Contract DE-AC05-76RL01830. S.A. acknowledges support from the National Science Foundation Graduate Research Fellowship Program under Grant No. DGE-1762114. This work was completed in part with resources provided by the University of Chicago Research Computing Center. We gratefully acknowledge computing time on the University of Chicago high-performance GPU-based cyberinfrastructure supported by the National Science Foundation under Grant No. DMR-1828629.

References

(1) Murphy, J. E.; Uno, T.; Hamer, J. D.; Cohen, F. E.; Dwarki, V.; Zuckermann, R. N. A combinatorial approach to the discovery of efficient cationic peptoid reagents for gene delivery. *Proc. Natl. Acad. Sci. U. S. A.* **1998**, *95*, 1517–1522.

(2) Wender, P. A.; Mitchell, D. J.; Pattabiraman, K.; Pelkey, E. T.; Steinman, L.; Rothbard, J. B. The design, synthesis, and evaluation of molecules that enable or enhance cellular uptake: peptoid molecular transporters. *Proc. Natl. Acad. Sci. U. S. A.* **2000**, *97*, 13003–13008.

(3) Sun, J.; Zuckermann, R. N. Peptoid polymers: a highly designable bioinspired material. *ACS Nano* **2013**, *7*, 4715–4732.

(4) Ghosh, C.; Manjunath, G. B.; Akkapeddi, P.; Yarlagadda, V.; Hoque, J.; Uppu, D. S.; Konai, M. M.; Haldar, J. Small molecular antibacterial peptoid mimics: the simpler the better! *J. Med. Chem.* **2014**, *57*, 1428–1436.

(5) Knight, A. S.; Zhou, E. Y.; Francis, M. B.; Zuckermann, R. N. Sequence programmable peptoid polymers for diverse materials applications. *Adv. Mater.* **2015**, *27*, 5665–5691.

(6) Bolt, H. L.; Eggimann, G. A.; Jahoda, C. A.; Zuckermann, R. N.; Sharples, G. J.; Cobb, S. L. Exploring the links between peptoid antibacterial activity and toxicity. *MedChemComm* **2017**, *8*, 886–896.

(7) Zuckermann, R. N. Peptoid origins. *Pept. Sci.* **2011**, *96*, 545–555.

(8) T Dohm, M.; Kapoor, R.; E Barron, A. Peptoids: bio-inspired polymers as potential pharmaceuticals. *Curr. Pharm. Des.* **2011**, *17*, 2732–2747.

(9) Jang, H.; Fafarman, A.; Holub, J. M.; Kirshenbaum, K. Click to fit: versatile polyvalent display on a peptidomimetic scaffold. *Org. Lett.* **2005**, *7*, 1951–1954.

(10) Weiser, L. J.; Santiso, E. E. Molecular modeling studies of peptoid polymers. *AIMS Mater. Sci.* **2017**, *4*, 1029.

(11) Yan, F.; Liu, L.; Walsh, T. R.; Gong, Y.; El-Khoury, P. Z.; Zhang, Y.; Zhu, Z.; De Yoreo, J. J.; Engelhard, M. H.; Zhang, X.; Chen, C.-L. Controlled synthesis of highly-branched plasmonic gold nanoparticles through peptoid engineering. *Nat. Commun.* **2018**, *9*, 1–8.

(12) Miller, S. M.; Simon, R. J.; Ng, S.; Zuckermann, R. N.; Kerr, J. M.; Moos, W. H. Comparison of the proteolytic susceptibilities of homologous L-amino acid, D-amino acid, and N-substituted glycine peptide and peptoid oligomers. *Drug Dev. Res.* **1995**, *35*, 20–32.

(13) Lee, J.; Udugamasooriya, D. G.; Lim, H.-S.; Kodadek, T. Potent and selective photo-inactivation of proteins with peptoid-ruthenium conjugates. *Nat. Chem. Biol.* **2010**, *6*, 258–260.

(14) Robertson, E. J.; Battigelli, A.; Proulx, C.; Mannige, R. V.; Haxton, T. K.; Yun, L.; Whitelam, S.; Zuckermann, R. N. Design, synthesis, assembly, and engineering of peptoid nanosheets. *Acc. Chem. Res.* **2016**, *49*, 379–389.

(15) Luo, Y.; Song, Y.; Wang, M.; Jian, T.; Ding, S.; Mu, P.; Liao, Z.; Shi, Q.; Cai, X.; Jin, H.; Du, D.; Dong, W.; Chen, C.; Lin, Y. Bioinspired peptoid nanotubes for targeted tumor cell imaging and chemo-photodynamic therapy. *Small* **2019**, *15*, 1902485.

(16) Song, Y.; Wang, M.; Li, S.; Jin, H.; Cai, X.; Du, D.; Li, H.; Chen, C.-L.; Lin, Y. Efficient cytosolic delivery using crystalline nanoflowers assembled from fluorinated peptoids. *Small* **2018**, *14*, 1803544.

(17) Nam, K. T.; Shelby, S. A.; Choi, P. H.; Marciel, A. B.; Chen, R.; Tan, L.; Chu, T. K.; Mesch, R. A.; Lee, B.-C.; Connolly, M. D.; Kisielowski, C.; Zuckermann, R. N. Free-

floating ultrathin two-dimensional crystals from sequence-specific peptoid polymers. *Nat. Mater.* **2010**, *9*, 454–460.

(18) Shao, L.; Ma, J.; Prelesnik, J. L.; Zhou, Y.; Nguyen, M.; Zhao, M.; Jenekhe, S. A.; Kalinin, S. V.; Ferguson, A. L.; Pfaendtner, J.; Mundy, C. J.; De Yoreo, J. J.; Baneyx, F.; Chen, C.-L. Hierarchical materials from high information content macromolecular building blocks: Construction, dynamic interventions, and prediction. *Chem. Rev.* **2022**, *122*, 17397–17478.

(19) Xuan, S.; Jiang, X.; Spencer, R. K.; Li, N. K.; Prendergast, D.; Balsara, N. P.; Zuckermann, R. N. Atomic-level engineering and imaging of polypeptoid crystal lattices. *Proc. Natl. Acad. Sci. U. S. A.* **2019**, *116*, 22491–22499.

(20) Rosales, A. M.; Murnen, H. K.; Zuckermann, R. N.; Segalman, R. A. Control of crystallization and melting behavior in sequence specific polypeptoids. *Macromolecules* **2010**, *43*, 5627–5636.

(21) Zuckermann, R. N.; Kerr, J. M.; Kent, S. B.; Moos, W. H. Efficient method for the preparation of peptoids [oligo (N-substituted glycines)] by submonomer solid-phase synthesis. *J. Am. Chem. Soc.* **1992**, *114*, 10646–10647.

(22) Li, Z.; Cai, B.; Yang, W.; Chen, C.-L. Hierarchical nanomaterials assembled from peptoids and other sequence-defined synthetic polymers. *Chem. Rev.* **2021**, *121*, 14031–14087.

(23) Davidson, E. C.; Rosales, A. M.; Patterson, A. L.; Russ, B.; Yu, B.; Zuckermann, R. N.; Segalman, R. A. Impact of helical chain shape in sequence-defined polymers on Polypeptoid block copolymer self-assembly. *Macromolecules* **2018**, *51*, 2089–2098.

(24) Greer, D. R.; Stolberg, M. A.; Kundu, J.; Spencer, R. K.; Pascal, T.; Prendergast, D.; Balsara, N. P.; Zuckermann, R. N. Universal relationship between molecular structure

and crystal structure in peptoid polymers and prevalence of the cis backbone conformation. *J. Am. Chem. Soc.* **2018**, *140*, 827–833.

(25) Hebert, M. L.; Shah, D. S.; Blake, P.; Turner, J. P.; Servoss, S. L. Tunable peptoid microspheres: effects of side chain chemistry and sequence. *Org. Biomol. Chem.* **2013**, *11*, 4459–4464.

(26) Murnen, H. K.; Rosales, A. M.; Jaworski, J. N.; Segalman, R. A.; Zuckermann, R. N. Hierarchical self-assembly of a biomimetic diblock copolypeptoid into homochiral superhelices. *J. Am. Chem. Soc.* **2010**, *132*, 16112–16119.

(27) Sanii, B.; Kudirka, R.; Cho, A.; Venkateswaran, N.; Olivier, G. K.; Olson, A. M.; Tran, H.; Harada, R. M.; Tan, L.; Zuckermann, R. N. Shaken, not stirred: collapsing a peptoid monolayer to produce free-floating, stable nanosheets. *J. Am. Chem. Soc.* **2011**, *133*, 20808–20815.

(28) Mannige, R. V.; Haxton, T. K.; Proulx, C.; Robertson, E. J.; Battigelli, A.; Butterfoss, G. L.; Zuckermann, R. N.; Whitelam, S. Peptoid nanosheets exhibit a new secondary-structure motif. *Nature* **2015**, *526*, 415–420.

(29) Nandakumar, A.; Ito, Y.; Ueda, M. Solvent effects on the self-assembly of an amphiphilic polypeptide incorporating α-helical hydrophobic blocks. *J. Am. Chem. Soc.* **2020**, *142*, 20994–21003.

(30) Castelletto, V.; Seitsonen, J.; Tewari, K. M.; Hasan, A.; Edkins, R. M.; Ruokolainen, J.; Pandey, L. M.; Hamley, I. W.; Lau, K. H. A. Self-assembly of minimal peptoid sequences. *ACS Macro Lett.* **2020**, *9*, 494–499.

(31) Lampel, A.; Ulijn, R.; Tuttle, T. Guiding principles for peptide nanotechnology through directed discovery. *Chem. Soc. Rev.* **2018**, *47*, 3737–3758.

(32) Frederix, P. W.; Scott, G. G.; Abul-Haija, Y. M.; Kalafatovic, D.; Pappas, C. G.; Javid, N.; Hunt, N. T.; Ulijn, R. V.; Tuttle, T. Exploring the sequence space for (tri-) peptide self-assembly to design and discover new hydrogels. *Nat. Chem.* **2015**, *7*, 30.

(33) Wei, G.; Su, Z.; Reynolds, N. P.; Arosio, P.; Hamley, I. W.; Gazit, E.; Mezzenga, R. Self-assembling peptide and protein amyloids: from structure to tailored function in nanotechnology. *Chem. Soc. Rev.* **2017**, *46*, 4661–4708.

(34) Vollrath, S. B.; Hu, C.; Bräse, S.; Kirshenbaum, K. Peptoid nanotubes: An oligomer macrocycle that reversibly sequesters water via single-crystal-to-single-crystal transformations. *Chem. Commun.* **2013**, *49*, 2317–2319.

(35) Cai, X.; Wang, M.; Mu, P.; Jian, T.; Liu, D.; Ding, S.; Luo, Y.; Du, D.; Song, Y.; Chen, C.-L.; Lin, Y. Sequence-defined nanotubes assembled from IR780-conjugated peptoids for chemophototherapy of malignant glioma. *Research* **2021**, *2021*, 9861384.

(36) Sun, J.; Jiang, X.; Lund, R.; Downing, K. H.; Balsara, N. P.; Zuckermann, R. N. Self-assembly of crystalline nanotubes from monodisperse amphiphilic diblock copolypeptoid tiles. *Proc. Natl. Acad. Sci. U. S. A.* **2016**, *113*, 3954–3959.

(37) Li, Z.; Tran, D. K.; Chem. Commun.Nguyen, M.; Jian, T.; Yan, F.; Jenekhe, S. A.; Chen, C.-L. Amphiphilic peptoid-directed assembly of oligoanilines into highly crystalline conducting nanotubes. *Macromol. Rapid Commun.* **2022**, *43*, 2100639.

(38) Jin, H.; Ding, Y.-H.; Wang, M.; Song, Y.; Liao, Z.; Newcomb, C. J.; Wu, X.; Tang, X.-Q.; Li, Z.; Lin, Y.; Yan, F.; Jian, T.; Mu, P.; Chen, C.-L. Designable and dynamic single-walled stiff nanotubes assembled from sequence-defined peptoids. *Nat. Commun.* **2018**, *9*, 1–11.

(39) Jin, H.; Jiao, F.; Daily, M. D.; Chen, Y.; Yan, F.; Ding, Y. H.; Zhang, X.; Robertson, E. J.; Baer, M. D.; Chen, C. L. Highly stable and self-repairing membrane-mimetic 2D nanomaterials assembled from lipid-like peptoids. *Nat. Commun.* **2016**, *7*, 1–8.

(40) Jiang, X.; Greer, D. R.; Kundu, J.; Ophus, C.; Minor, A. M.; Prendergast, D.; Zuckermann, R. N.; Balsara, N. P.; Downing, K. H. Imaging unstained synthetic polymer crystals and defects on atomic length scales using cryogenic electron microscopy. *Macromolecules* **2018**, *51*, 7794–7799.

(41) Zhao, M.; Lachowski, K. J.; Zhang, S.; Alamdari, S.; Sampath, J.; Mu, P.; Mundy, C. J.; Pfaendtner, J.; De Yoreo, J. J.; Chen, C.-L.; Pozzo, L. D.; Ferguson, A. L. Hierarchical self-assembly pathways of peptoid helices and sheets. *Biomacromolecules* **2022**, *23*, 992–1008.

(42) Mu, P.; Zhou, G.; Chen, C.-L. 2D nanomaterials assembled from sequence-defined molecules. *Nano-Struct. Nano-Objects* **2018**, *15*, 153–166.

(43) Ma, J.; Cai, B.; Zhang, S.; Jian, T.; De Yoreo, J. J.; Chen, C.-L.; Baneyx, F. Nanoparticle-mediated assembly of peptoid nanosheets functionalized with solid-binding proteins: Designing heterostructures for hierarchy. *Nano Lett.* **2021**, *21*, 1636–1642.

(44) Monahan, M.; Cai, B.; Jian, T.; Zhang, S.; Zhu, G.; Chen, C.-L.; De Yoreo, J. J.; Cossairt, B. M. Peptoid-directed assembly of CdSe nanoparticles. *Nanoscale* **2021**, *13*, 1273–1282.

(45) Hanwell, M. D.; Curtis, D. E.; Lonie, D. C.; Vandermeersch, T.; Zurek, E.; Hutchison, G. R. Avogadro: an advanced semantic chemical editor, visualization, and analysis platform. *J. Cheminf.* **2012**, *4*, 1–17.

(46) Weiser, L. J.; Santiso, E. E. A CGenFF-based force field for simulations of peptoids with both cis and trans peptide bonds. *J. Comput. Chem.* **2019**, *40*, 1946–1956.

(47) Mackerell, A. D.; Feig, M.; Brooks, C. L. Extending the treatment of backbone energetics in protein force fields: limitations of gas-phase quantum mechanics in reproduc-

ing protein conformational distributions in molecular dynamics simulation. *J. Comput. Chem.* **2004**, *25*, 1400–1415.

(48) Best, R. B.; Zhu, X.; Shim, J.; Lopes, P. E.; Mittal, J.; Feig, M.; MacKerell, A. D. Optimization of the additive CHARMM all-atom protein force field targeting improved sampling of the backbone ϕ, ψ and side-chain $\chi 1$ and $\chi 2$ Dihedral Angles. *J. Chem. Theory Comput.* **2012**, *8*, 3257–3273.

(49) Mirijanian, D. T.; Mannige, R. V.; Zuckermann, R. N.; Whitelam, S. Development and use of an atomistic CHARMM-based forcefield for peptoid simulation. *J. Comput. Chem.* **2014**, *35*, 360–370.

(50) Hoyas, S.; Lemaur, V.; Duez, Q.; Saintmont, F.; Halin, E.; De Winter, J.; Gerbaux, P.; Cornil, J. PEPDROID: Development of a generic DREIDING-based force field for the assessment of peptoid secondary structures. *Adv. Theory Simul.* **2018**, *1*, 1800089.

(51) Perrin, D. D. *Dissociation constants of organic bases in aqueous solution: supplement 1972*; Franklin Book Company, 1972; Vol. 1.

(52) Liang, T.; Shin, Y. K.; Cheng, Y.-T.; Yilmaz, D. E.; Vishnu, K. G.; Verners, O.; Zou, C.; Phillpot, S. R.; Sinnott, S. B.; Van Duin, A. C. Reactive potentials for advanced atomistic simulations. *Annu. Rev. Mater. Res.* **2013**, *43*, 109–129.

(53) Chen, W.; Morrow, B. H.; Shi, C.; Shen, J. K. Recent development and application of constant pH molecular dynamics. *Mol. Simul.* **2014**, *40*, 830–838.

(54) Jorgensen, W. L.; Chandrasekhar, J.; Madura, J. D.; Impey, R. W.; Klein, M. L. Comparison of simple potential functions for simulating liquid water. *J. Chem. Phys.* **1983**, *79*, 926–935.

(55) Martínez, L.; Andrade, R.; Birgin, E. G.; Martínez, J. M. PACKMOL: a package for

building initial configurations for molecular dynamics simulations. *J. Comput. Chem.* **2009**, *30*, 2157–2164.

(56) Páll, S.; Abraham, M. J.; Kutzner, C.; Hess, B.; Lindahl, E. Tackling exascale software challenges in molecular dynamics simulations with GROMACS. International Conference on Exascale Applications and Software. 2014; pp 3–27.

(57) Abraham, M. J.; Murtola, T.; Schulz, R.; Páll, S.; Smith, J. C.; Hess, B.; Lindahl, E. GROMACS: High performance Mol. Simul.s through multi-level parallelism from laptops to supercomputers. *SoftwareX* **2015**, *1*, 19–25.

(58) Bussi, G.; Donadio, D.; Parrinello, M. Canonical sampling through velocity rescaling. *J. Chem. Phys.* **2007**, *126*, 14101.

(59) Berendsen, H. J.; Postma, J. P.; Van Gunsteren, W. F.; Dinola, A.; Haak, J. R. Molecular dynamics with coupling to an external bath. *J. Chem. Phys.* **1984**, *81*, 3684–3690.

(60) Nosé, S. A unified formulation of the constant temperature molecular dynamics methods. *J. Chem. Phys.* **1984**, *81*, 511–519.

(61) Parrinello, M.; Rahman, A. Polymorphic transitions in single crystals: a new molecular dynamics method. *J. Appl. Phys.* **1981**, *52*, 7182–7190.

(62) Hockney, R. W.; Eastwood, J. W. *Computer Simulation Using Particles*; CRC Press, 1988.

(63) Hess, B.; Bekker, H.; Berendsen, H. J.; Fraaije, J. G. LINCS: A linear constraint solver for Mol. Simul.s. *J. Comput. Chem.* **1997**, *18*, 1463–1472.

(64) Essmann, U.; Perera, L.; Berkowitz, M. L.; Darden, T.; Lee, H.; Pedersen, L. G. A smooth particle mesh Ewald method. *J. Chem. Phys.* **1995**, *103*, 8577–8593.

(65) Humphrey, W.; Dalke, A.; Schulten, K. VMD: visual molecular dynamics. *J. Mol. Graphics* **1996**, *14*, 33–8.

(66) Fang, T.-H.; Weng, C.-I.; Chang, J.-G. Molecular dynamics analysis of temperature effects on nanoindentation measurement. *Mater. Sci. Eng.: A* **2003**, *357*, 7–12.

(67) Fang, T.-H.; Wu, J.-H. Molecular dynamics simulations on nanoindentation mechanisms of multilayered films. *Comput. Mater. Sci.* **2008**, *43*, 785–790.

(68) Goel, S.; Joshi, S. S.; Abdelal, G.; Agrawal, A. Molecular dynamics simulation of nanoindentation of Fe3C and Fe4C. *Mater. Sci. Eng.: A* **2014**, *597*, 331–341.

(69) Ruestes, C. J.; Bringa, E. M.; Gao, Y.; Urbassek, H. M. Molecular dynamics modeling of nanoindentation. *Appl. Nanoindentation Adv. Mater.* **2017**, 313–345.

(70) Zhong, T.; Li, J.; Zhang, K. A molecular dynamics study of Young's modulus of multilayer graphene. *J. Appl. Phys.* **2019**, *125*, 175110.

(71) Tan, X.; Wu, J.; Zhang, K.; Peng, X.; Sun, L.; Zhong, J. Nanoindentation models and Young's modulus of monolayer graphene: A molecular dynamics study. *Appl. Phys. Lett.* **2013**, *102*, 071908.

(72) Kontomaris, S.; Malamou, A. Hertz model or Oliver & Pharr analysis? Tutorial regarding AFM nanoindentation experiments on biological samples. *Mater. Res. Express* **2020**, *7*, 033001.

(73) Kuznetsov, V.; Zinn, A.-H.; Zampardi, G.; Borhani-Haghighi, S.; La Mantia, F.; Ludwig, A.; Schuhmann, W.; Ventosa, E. Wet nanoindentation of the solid electrolyte interphase on thin film Si electrodes. *ACS Appl. Mater. Interfaces* **2015**, *7*, 23554–23563.

(74) Greaves, G. N.; Greer, A. L.; Lakes, R. S.; Rouxel, T. Poisson's ratio and modern materials. *Nat. Mater.* **2011**, *10*, 823–837.

(75) McKee, C. T.; Last, J. A.; Russell, P.; Murphy, C. J. Indentation versus tensile measurements of Young's modulus for soft biological tissues. *Tissue Eng., Part B* **2011**, *17*, 155–164.

(76) Manevitch, O. L.; Rutledge, G. C. Elastic properties of a single lamella of montmorillonite by molecular dynamics simulation. *J. Phys. Chem. B* **2004**, *108*, 1428–1435.

(77) Hu, M.; Diggins IV, P.; Deserno, M. Determining the bending modulus of a lipid membrane by simulating buckling. *J. Chem. Phys.* **2013**, *138*, 214110.

(78) Diggins IV, P.; McDargh, Z. A.; Deserno, M. Curvature softening and negative compressibility of gel-phase lipid membranes. *J. Am. Chem. Soc.* **2015**, *137*, 12752–12755.

(79) Eid, J.; Razmazma, H.; Jraij, A.; Ebrahimi, A.; Monticelli, L. On calculating the bending modulus of lipid bilayer membranes from buckling simulations. *J. Phys. Chem. B* **2020**, *124*, 6299–6311.

(80) Sun, D.; Shu, D.; Ji, M.; Liu, F.; Wang, M.; Gong, X. Pressure-induced hard-to-soft transition of a single carbon nanotube. *Phys. Rev. B* **2004**, *70*, 165417.

(81) Yang, Y.; Gao, Y.; Sun, D.; Asta, M.; Hoyt, J. Capillary force induced structural deformation in liquid infiltrated elastic circular tubes. *Phys. Rev. B* **2010**, *81*, 241407.

(82) Stottrup, B. L.; Heussler, A. M.; Bibelnieks, T. A. Determination of Line Tension in Lipid Monolayers by Fourier Analysis of Capillary Waves. *J. Phys. Chem. Lett.* **2007**, *111*, 11091–11094.

(83) Tüzel, E.; Pan, G.; Kroll, D. M. Dynamics of thermally driven capillary waves for two-dimensional droplets. *J. Chem. Phys.* **2010**, *132*, 174701.

(84) Virtanen, P.; Gommers, R.; Oliphant, T. E.; Haberland, M.; Reddy, T.; Cournapeau, D.; Burovski, E.; Peterson, P.; Weckesser, W.; Bright, J.; van der Walt, S. J.; Brett, M.; Wilson, J.; Millman, K. J.; Mayorov, N.; Nelson, A. R. J.; Jones, E.; Kern, R.;

Larson, E.; Carey, C. J.; Polat, İ.; Feng, Y.; Moore, E. W.; VanderPlas, J.; Laxalde, D.; Perktold, J.; Cimrman, R.; Henriksen, I.; Quintero, E. A.; Harris, C. R.; Archibald, A. M.; Ribeiro, A. H.; Pedregosa, F.; van Mulbregt, P.; SciPy 1.0 Contributors, SciPy 1.0: Fundamental Algorithms for Scientific Computing in Python. *Nat. Methods* **2020**, *17*, 261–272.

(85) Robertson, E. J.; Proulx, C.; Su, J. K.; Garcia, R. L.; Yoo, S.; Nehls, E. M.; Connolly, M. D.; Taravati, L.; Zuckermann, R. N. Molecular engineering of the peptoid nanosheet hydrophobic core. *Langmuir* **2016**, *32*, 11946–11957.

(86) Murray, D. J.; Kim, J. H.; Grzincic, E. M.; Kim, S. C.; Abate, A. R.; Zuckermann, R. N. Uniform, large-area, highly ordered peptoid monolayer and bilayer films for sensing applications. *Langmuir* **2019**, *35*, 13671–13680.

(87) Akaike, H. In *Selected Papers of Hirotugu Akaike*; Parzen, E., Tanabe, K., Kitagawa, G., Eds.; Springer Series in Statistics, 1998; Chapter Information theory and an extension of the maximum likelihood principle, pp 199–213.

TOC Graphic